Journal of the European Ceramic Society 43 (2023) 362–369

Contents lists available at ScienceDirect

Journal of the European Ceramic Society

journal homepage: www.elsevier.com/locate/jeurceramsoc

Structural investigation of the temperature-stable relaxor dielectric $Ba_{0.8}Ca_{0.2}TiO_3$-$Bi(Mg_{0.5}Ti_{0.5})O_3$

M. Cabral [a], A.P. Brown [b,*], J. Bultitude [c], A. Britton [b], R. Brydson [b], T. Roncal-Herrero [b], D.A. Hall [d], S.J. Milne [b,*], A.M. Rappe [e], D.C. Sinclair [f], J. Zhang [e], Y. Li [d]

[a] North Carolina State University, 911 Partners Way, Engineering Building 1, Room 3002, Raleigh NC, 27695, USA
[b] School of Chemical and Process Engineering, University of Leeds, Leeds LS6 2BD, UK
[c] KEMET Ceramic innovation Centre, 2835 KEMET Way, Simpsonville, SC 29681, USA
[d] Department of Materials, MSS Building, University of Manchester, Manchester M13 9PL, UK
[e] Department of Chemistry, University of Pennsylvania, Philadelphia, PA 19104-6323, USA
[f] Department of Materials Science and Engineering, University of Sheffield, Mappin St., Sheffield S1 3JD, UK

ARTICLE INFO

Keywords:
Microstructure
Nanostructure
Structure-Property Relationships
Dielectrics
X-ray
Diffraction

ABSTRACT

Aberration corrected scanning transmission electron microscopy (STEM) and electron diffraction have been used to disclose local structure and nano-chemistry in a Ca modified $BaTiO_3$-$Bi(Mg_{0.5}Ti_{0.5})O_3$ relaxor dielectric ceramic which exhibits high and near-invariant relative permittivity over a wide temperature range. High-resolution, synchrotron X-ray diffraction indicated a globally cubic structure ($Pm\bar{3}m$), but direct atomic-scale imaging by STEM revealed local tetragonal distortions. Nanopolar clusters were identified from *B*-site atomic displacement vectors measured relative to oxygen ion positions along $< 100 >$ and $< 110 >$ zone axes of integrated differential phase contrast (iDPC) STEM images, highlighting cluster sizes of 2–5 nm. Chemical analysis by STEM-energy dispersive X-ray spectroscopy and full pattern refinements of X-ray powder diffraction data each implied high levels of Bi vacancies within the matrix. The possibility that these A-site vacancies modulate the nanopolar structure and promote flattening of the permittivity-temperature response in this class of dielectric is discussed.

1. Introduction

Research into dielectric ceramics with high and near-stable relative permittivity to temperatures exceeding 200 °C is motivated by the need to develop new types of Class II capacitors for use in power and harsh environment electronics. New wide-bandgap semiconductor technologies based on SiC and GaAs demonstrate the potential to provide active components that can operate at 250–300 °C allowing reductions in heatsink size and equipment weight [1]. Due to the much higher switching speeds of wide-bandgap devices in power electronic equipment, passive and active components must be in close proximity (e.g. co-packaged), demanding high temperature operation of passive components within high voltage circuits. Existing commercially available Class II capacitors based on ferroelectric $BaTiO_3$ only operate reliably to $\leq$ 200 °C and are unsuitable for emerging power applications such as transport electrification. There are also requirements for 250–300 °C capable capacitors where the electronic circuits are located in high ambient temperature environments, for example engine control and sensing systems, or deep well drilling operations [2].

In response to these technological demands, there has been intense research activity in recent years into next generation Class-II dielectric ceramics. New materials and devices must maintain high dielectric charge storage to upper working temperatures of 250–300 °C. They must also conform to the Electronics Industries Alliance (EIA) R-type specification, such that, capacitance varies by no more than ± 15 % across the full temperature range.

To date, materials that best fulfil this role are perovskite-structured, relaxor dielectrics for example, compositions within the solid solution series: $BaTiO_3$-$BiScO_3$ and $BaTiO_3$-$Bi(M'_{0.5}Ti_{0.5})O_3$, where M′ = Mg or Zn [3–6].

Frequency relaxation and a diffuse permittivity-temperature response distinguish relaxors from classical ferroelectrics such as $BaTiO_3$. The behaviour is most commonly attributed to the formation of nanoscale polar domains or clusters, commonly referred to as “polar

* Corresponding authors.
E-mail addresses: a.p.brown@leeds.ac.uk (A.P. Brown), S.J.Milne@leeds.ac.uk (S.J. Milne).

https://doi.org/10.1016/j.jeurceramsoc.2022.09.039
Received 11 April 2022; Received in revised form 13 September 2022; Accepted 20 September 2022
Available online 22 September 2022

nano-regions" (PNRs) or polar nano-clusters, in contrast to the micrometre sized domains of traditional ferroelectrics [7–13]. The phenomenon has been studied extensively in the prototypical relaxor ferroelectric solid solution $Pb(Mg_{1/3}Nb_{2/3})O_3$-$PbTiO_3$ (PMN-PT) where PNRs are theorized to form when cooling through the characteristic Burns temperature (T_B) [7–13]. Structural changes resulting from local compositional heterogeneity and consequent charge and atomic radii mismatches are generally thought to give rise to fluctuating electrostatic and stress fields that inhibit long-range dipole coupling in a relaxor ferroelectric. The broad frequency-dependent maximum in the relative permittivity-temperature response of these materials is considered to be a result of thermally-induced changes to polar coupling (within/between PNRs), combined with changes to dipole reorientation dynamics.

The permittivity peak has been shown to become even more diffuse in relaxors based on $BaTiO_3$ modified by Bi-containing perovskites such as $BiScO_3$, $Bi(Mg_{0.5}Ti_{0.5})O_3$ or $Bi(Zn_{0.5}Ti_{0.5})O_3$ [3–5]. For compositions approaching the solid solution limits, a near-flat permittivity-temperature response is obtained over wide temperature ranges. Consequently, the EIA standard of ± 15 % consistency in capacitance can be extended to upper temperatures well in excess of 300 °C. This type of material is of potential interest for next-generation Class II multilayer ceramic capacitors, particularly for applications where the requirement for high-cost internal Ag-Pd electrodes is acceptable. Moreover, a near linear polarisation-electric field response is retained to high fields making it possible to achieve relatively high energy storage densities in microstructurally dense, thin or thick-film ceramics with high dielectric breakdown strengths [6].

The reasons for this change from a normal relaxor response to a temperature- insensitive response are not fully understood [14–16]. Here we report results of atomic column resolution, aberration-corrected imaging and analysis of nano-chemistry using scanning transmission electron microscopy (STEM), together with high-resolution X-ray powder diffraction, to probe the link between atom displacements and chemical mapping in the temperature-stable relaxor: $(1\text{-}x)Ba_{0.8}Ca_{0.2}TiO_3$ -$xBiMg_{0.5}Ti_{0.5}O_3$, x = 0.5 (0.5BCT-0.5BMT). The composition lies close to the solid solution limit [17,18].

2. Methods

The ceramic sample was prepared by the mixed oxide powder route. Starting reagents were $CaCO_3$ (Sigma Aldrich, 99 % purity,St. Louis, MO), TiO_2 (Sigma Aldrich, 99.9 %), $BaCO_3$ (Alpha Aesar, 99 %, Ward Hill, MA), MgO (Alpha Aesar,99.9 %), and Bi_2O_3 (Alpha Aesar, 99 %). Reagents were dried at 250 °C overnight, before cooling to room temperature in a desiccator and weighed according to stoichiometric ratios. Powders were mixed by ball-milling for 24 h overnight in isopropanol using stabilized zirconia grinding media. The powders were dried, calcined at 900 °C for 3 h and then ball-milled again for 24 h before. Milled powder were formed into pellets by uniaxial pressing in a 10 mm steel die at 65 MPa, followed by cold isostatic pressing at 300 MPa. A binder (Ciba Glascol HA4; Ciba Speciality Chemicals, Bradford, UK) was introduced during the post-calcination milling stage. The pellets were embedded in powder of the same composition and sintered at 1100 °C for 3 h [17,18] in a closed alumina crucible with the intention of minimizing loss of volatile bismuth oxide.

High-resolution synchrotron X-ray powder diffraction (HR-XRD) of a crushed sintered pellet was performed at Beamline I11, Diamond Light Source UK. The diffraction pattern was collected from a powder sample, sealed in 0.3 mm diameter borosilicate glass capillary, with a beam wavelength of 0.82657 Å and multi-analysing crystal (MAC) detectors. Crystal structural refinement using the Rietveld method was conducted using the Topas 5 software. The profile was fitted with a Chebychev background function and a pseudo Voigt profile function over the 2θ angular range 5° to 100°. The instrumental contribution to the profile was preset by refinement of peak shape parameters of a standard Si sample XRD profile.

Samples were prepared for electron microscopy via mechanical wedge polishing (Allied™ Multiprep) to a thickness of ~40 μm followed by low energy Ar^+ ion milling to electron transparency (Fischione™ 1050 ion mill). This preparation technique ensures ultrathin samples with minimal surface damage (< 20 nm thick) [19]. Imaging was performed on a probe-corrected FEI Titan G2 80–300 S/TEM operated at 200 kV with an electron probe semi-angle of convergence of 19.6 mrad. Annular dark-field (ADF) images were collected using a detector semi-angle range of 28–180 mrad, while integrated differential phase contrast (iDPC) images were collected with a detector semi-angle range of 7–28 mrad on FEI's four quadrant detector. To correct for scanning distortion, two 1024 × 1024 pixel (10 μs/pixel dwell time) images were acquired with orthogonal scan directions and were corrected during post-processing procedures [20]. Atom column positions were determined using atom column indexing [21] and Atomap [22] with further analysis being performed using custom Matlab and Python scripts. The STEM elemental X-ray maps were acquired using the SuperX Energy Dispersive X-ray Spectroscopy (EDS) detectors of the microscope and processed within the Velox software.

3. Results

The HR-XRD data were refined to a cubic system ($Pm\bar{3}m$), with lattice parameter, $a = 3.992(3)$ Å (Fig. 1): best-fit refinement parameters and site occupancies are presented in Table 1.

The R_{wp} values of trial refinements decreased from 11.01 % to 9.91 % by: (i) introducing Bi deficiency into the model; (ii) varying the thermal displacement parameters, B_{iso} and U_{iso} for different A-site elements. The latter resulted in significantly increased values of thermal displacement parameters for bismuth ions, to 5.73 $Å^2$ (B_{iso}) and 0.27 Å (*U*iso), Table 1. The fitting profiles of each iteration are shown in Fig. 2a and b.

The corresponding chemical formula for the Rietveld refinement with the lowest R_{wp} value was determined to be $Ba_{0.4}Ca_{0.1}Bi_{0.41}Ti_{0.75}Mg_{0.25}O_{2.865}\mathbf{V_{Bix}V_{Oy}}$ (from the refinement parameters listed in Table 1), with *x* Bi ion vacancies, $\mathbf{V_{Bix}} = 0.09$ and *y* oxygen vacancies, $\mathbf{V_{Oy}} = 0.135$ for charge balance. Although such a high level of bismuth deficiency is unusual (at ~16 at% of the Bi sites), the value is consistent with the observation of Bi-loss in a similar composition, 0.45BCT-0.55BMT identified by a previous TEM-EDS study and is verified below by TEM-EDS for this 0.5BCT-0.5BMT [18].

The nanoscale crystal structure of 0.5BCT-0.5BMT was revealed by atom-resolution STEM images acquired along the pseudocubic [100] and [110] zone axes from a ceramic section ~ 20 nm in thickness (Fig. 3). The as-acquired ADF images are shown with fast Fourier Transforms (FFTs) of the images inset (Fig. 3a and b; streaking in the FFTs is an artefact due to the appearance of the sharp discontinuity between intensities at the image edge). Also shown are the corresponding selected area electron diffraction (SAED) patterns from each axis (Fig. 3c and d). The SAEDs were indicative of a globally cubic structure, with weak diffuse scattering along < 110 > apparent for the [100] orientated grains because of the appearance of slight streaking along the body diagonals of the [100] pattern (Fig. 3c). Similarly, diffuse electron scattering, possibly originating from asymmetric Bi-O bonding in the {111} planes, is reported for other Bi-based perovskites [16].

In order to capture each sub-lattice position, simultaneous ADF and iDPC images were acquired for both zone axes (Fig. 4a-d, respectively). Cation displacements (B-sites) have in the past been obtained by measuring B-site atom positions relative to A-site cation positions in ADF images. Ferroelectric polarization is however, more appropriately defined as the displacement of cations with respect to oxygen positions. iDPC STEM can visualise all atom positions, since the atomic contrast in iDPC only varies linearly with atomic number [23]. Thus, by

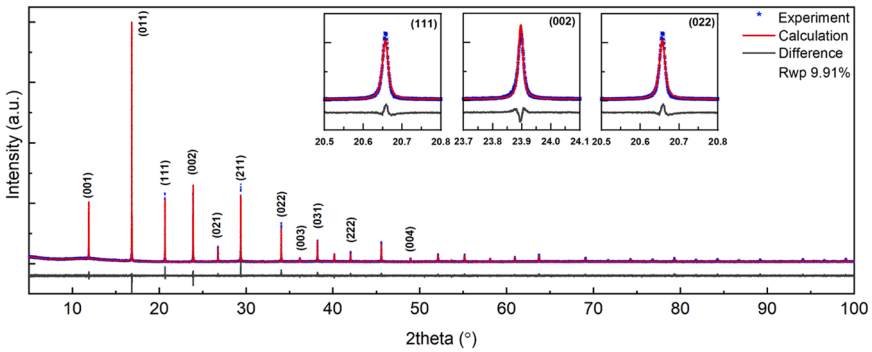

Fig. 1. HR-XRD profile and corresponding Rietveld refinement results for 0.5BCT-0.5BMT, incorporating a model of a simple cubic structure refined with bismuth deficiency and increased thermal parameter, B_{iso}, for A-site elements (see also Figure 2).

Table 1
Atom coordinates and isotropic thermal parameters (B_{iso} and u_{iso}) from full pattern refinement of 0.5BCT-0.5BMT. Note: (i) the deficiency in Bi occupancy (0.41 experimental) relative to a stoichiometric composition (0.5 calculated) and (ii) the high thermal displacement parameters for Bi ions on the A-sites.

Atom	Wycoff Positions	x	y	z	Occupancy Calc. Expt.	B_{iso}/Å^2	u_{iso}/ Å
Ba	1	0	0	0	0.4 *0.4*	0.70 (2)	0.094
Ca	1	0	0	0	0.1 *0.1*	0.70 (2)	0.094
Bi	1	0	0	0	0.5 *0.41*	5.73 (6)	0.27
Ti	1	0.5	0.5	0.5	0.75 *0.75*	0.11 (1)	0.037
Mg	1	0.5	0.5	0.5	0.25 *0.25*	0.11 (1)	0.037
O	3	0.5	0	0.5	*1.0* 0.955	0.15 (3)	0.044

successfully imaging oxygen anion and cation positions (Fig. 4c and d) we were able to determine average cation displacements with respect to the oxygen anions. Atomic displacement vectors were produced by subtracting the centroid of the *A* and *B* sub-lattice positions from the centroid of the oxygen positions in each projected cell visible in images analysed along the < 100 > and < 110 > zone axes, as shown by the red arrows in Fig. 5a and b respectively. Specifically, for the < 100 > zone axis, the polar cation displacements were calculated by averaging four A sub-lattice positions with the position of a B sub-lattice atomic column and subtracting this from the average position of the four oxygen columns in each unit cell. Likewise, the average cation displacement was calculated for the < 110 > zone axis by using the average position of one A sub-lattice and two B sub-lattice positions and subtracting the average position of four oxygen atom columns. These cation displacement 'polarization' maps indicate local polar clusters 2–5 nm in size (Fig. 5) for a material with an average 'cubic' unit cell, edge length of 0.3992 nm by XRD (Fig. 1).

As intimated in the Introduction, polar clusters or nanoregions have been widely theorised as the key determinant of relaxor-like ferroelectric behaviour in a number of multicomponent oxide systems. Here our

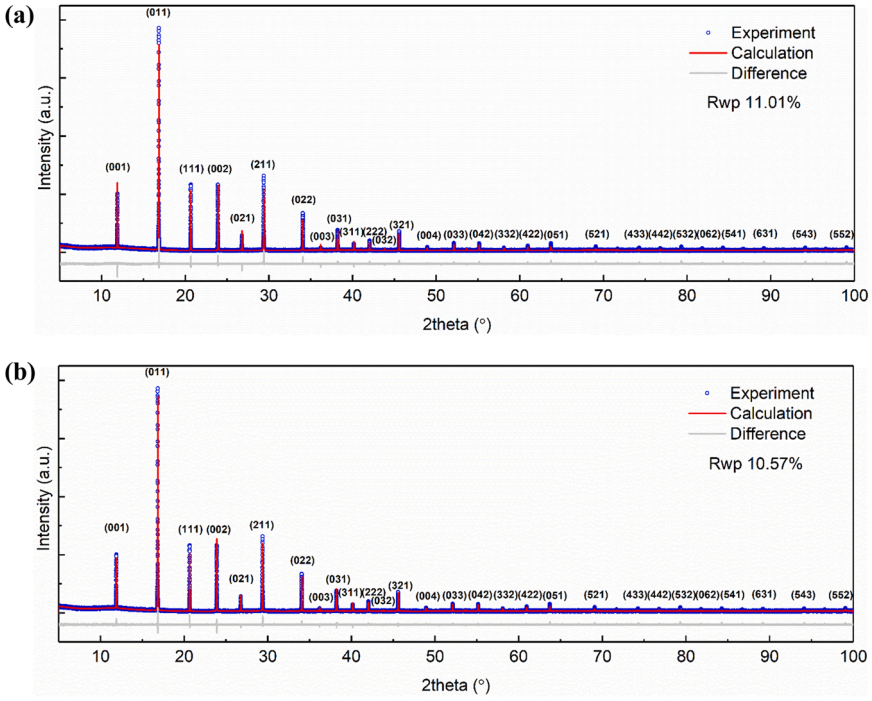

Fig. 2. HR-XRD profiles and corresponding Rietveld refinement results for the 0.5BCT-0.5BMT ceramic: (a) incorporating a model of simple cubic structure with a composition of 0.5BCT-0.5BMT; (b) incorporating a model of simple cubic structure with the refinement of bismuth deficiency (see Table 1).

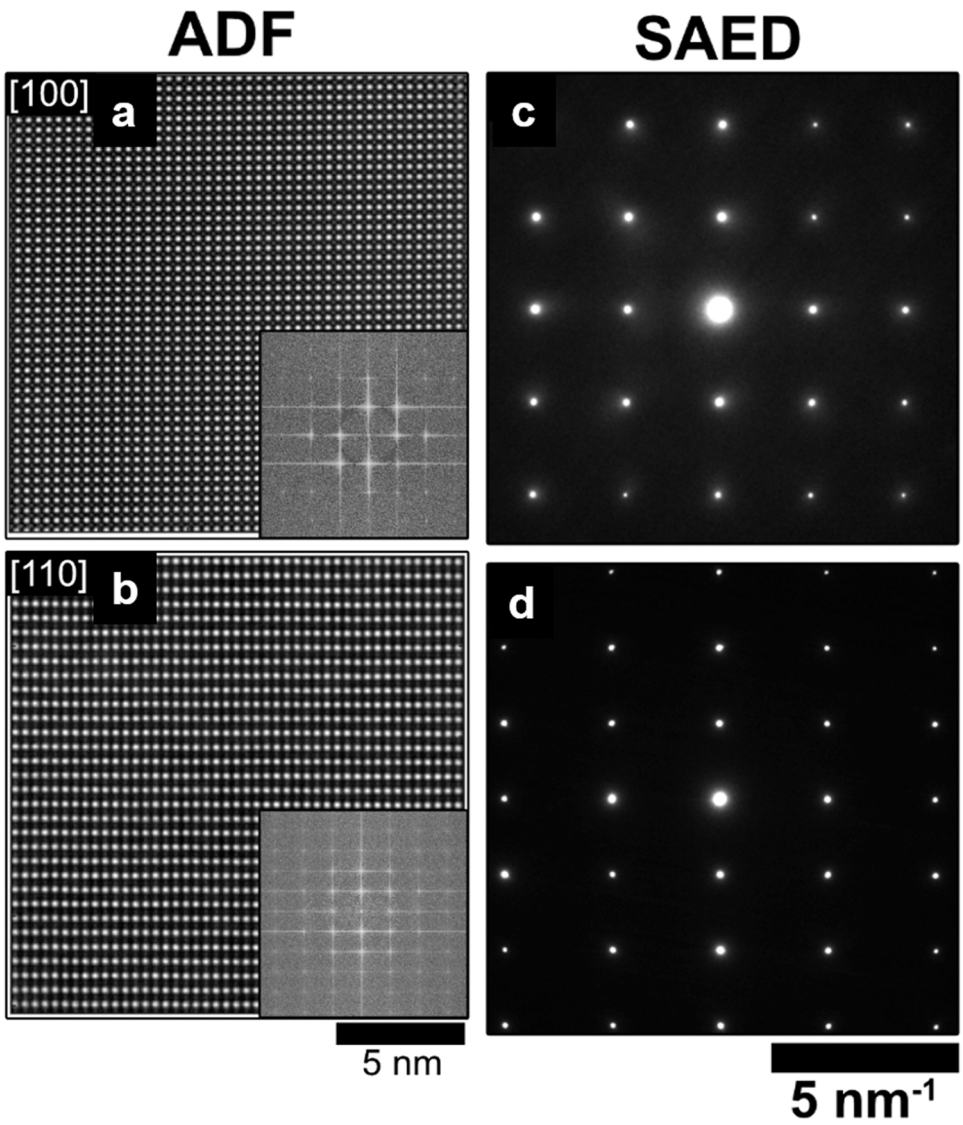

Fig. 3. As-acquired, annular dark-field (ADF) images for the (a) [100] and (b) [110] zone axes of 0.5BCT-0.5BMT (inset are the fast Fourier Transforms of the image; streaking result from image edge effects). Corresponding selected area electron diffraction (SAED) patterns for the (c) [100] and (d) [110] zone axes of 0.5BCT-0.5BMT (diffuse electron scatter is visible as slight streaking along the body diagonals of (c) the [100] pattern).

STEM iDPC imaging provides convincing *direct* visual evidence of nanopolar clusters within BCT-BMT (Fig. 5). Although polarization direction tends to vary between each cluster, or polar nanoregion, the largest displacement vectors occur along or close to the < 100 > type directions, indicating local tetragonal distortions.

The ADF-images can provide additional evidence of variations in the local structure for each sub lattice by extracting the normalized column intensities and c/a ratios for each projected unit cell along < 100 > to give a measurement of the local tetragonality and highlight any compositional relationships. Atom column intensity will be discussed in the next paragraph (and variation shown for B sub-lattice sites in Fig. 6a). The unit cell c/a ratios determined from the *B* sub-lattice positions are shown in Fig. 6b. Individual unit cells showed tetragonal distortions, with measured c/a ratios up to a maximum of 1.1. However, measured over many images, the mean c/a ratio was determined to be unity, consistent with the HR-XRD data of a globally cubic structure (Fig. 1). The standard deviation in c/a ratio based on the *B*-site sub-lattice was 0.02 (Fig. 6a), as opposed to 0.001 for *A*-site sub-lattice measurements (data not shown). The much higher deviation based on *B*-sites indicates a greater local variability in *B*-site displacement (tetragonality) between unit cells, as might be expected from the different displacement characteristics of the B-site ions; typically Mg shows little off-centre displacement compared to Ti [24,25].

Given the strong mass contrast of ADF imaging, the existence of any nanoscale chemical segregation (atom column intensity) that might affect polar structure, for example, dipole coupling length scales should be evident for this ceramic formulation [26,27]. Detailed inspection of the atom column intensities in ADF images was performed by measuring the peak intensities with a 2D Gaussian fit of each atom column [21]. An intensity variation of approximately ± 10 % was observed for the *A* sub-lattice indicating that local chemical order on the sub 10 nm length scale explored via STEM in this study, is not present to any significant level or is masked by the high level of Bi vacancies distributed across A-site columns. The B sub-lattice intensities cover a much broader range of ± 30 % of the mean value (Fig. 6a), despite the constituent elements having a more comparable range of Z values. This greater deviation could originate from the differing displacement characteristics of Ti relative to Mg ions. There was however, no clear correlation between variations in column intensity and variations in c/a ratio.

Super lattice reflections were absent from SAED patterns of 0.5BCT-0.5BMT (Fig. 3a and b). Thus, there was no evidence of short-range periodic ordering of Ti and Mg ions. This contrasts to the case of Nb

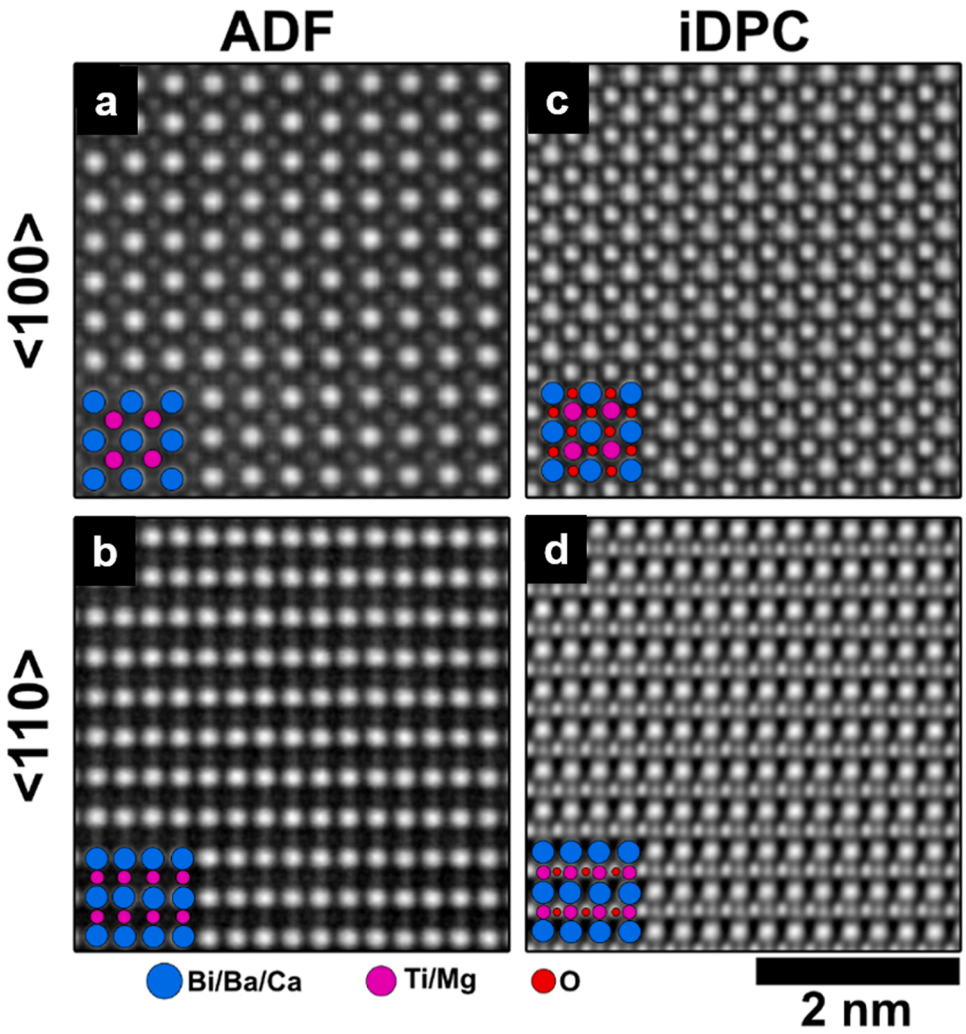

Fig. 4. Scan distortion corrected, annular dark-field (ADF) images for the (a) < 100 > and (b) < 110 > zone axes of 0.5BCT-0.5BMT. Integrated differential phase contrast (iDPC) images for the (c) < 100 > and (d) < 110 > zone axes. Projected atomic positions of the X-ray structure of 0.5BCT-0.5BMT are shown overlaid; note the identification of O positions (red) in the iDPC images.

and Mg ions in PMN-PT relaxor ferroelectrics where B-site periodicity takes the form of alternating Mg and Nb rich layers, giving rise to super lattice reflections in diffraction patterns acquired along < 110 > zone axes [27–30].

Longer-range microstructural information was obtained by STEM-EDS, Fig. 7. This highlighted Bi enrichment at grain boundaries and local regions of Ba and Ti enrichment, in agreement with our earlier report [18]. The atomic percentage of Bi *relative to all cations* was estimated by semi-quantitative analysis of EDS spectra to be ~20 at% within grains and ~30 at% at the grain boundary regions i.e. Bi deficient within grains (Fig. 7). Grain sizes were less than ~2–3 μm.

4. Discussion

The HR-XRD diffraction profile of the single - phase sample was initially refined with a cubic perovskite structure ($Pm\bar{3}m$) for the nominal composition of 0.5BCT-0.5BMT. Thereafter, more refinement parameters were introduced stepwise, namely: bismuth deficiency; magnesium deficiency; variation in thermal parameter, B_{iso}, of A-site and B-site elements. The best fit was found for the refinement considering both bismuth deficiency and an increased thermal parameter, B_{iso}, for all A-site elements, as shown in Fig. 1. Refinements of magnesium deficiency showed no improvement in the goodness of fit.

For compositions in related solid solution systems, $BaTiO_3$-$BiScO_3$ and $BaTiO_3$-$Bi(Zn_{0.5}Ti_{0.5})_3$, other investigators have found correlations of Bi and Ti displacements, and local tetragonal distortions over a few unit cell length scales, in a globally cubic structure by using a combination of high resolution X-ray, neutron, and electron diffuse scattering supported by Reverse Monte Carlo simulations [14–16]. We have also observed this correlation in 0.5BCT-0.5BMT. However our work shows no clear correlation between the magnitude of the correlated polar clusters and local chemistry in 0.5BCT-0.5BMT, as there is no obvious correlation between (changing) atom column intensities along < 100 > and the cation displacement orientations on the length scales imaged here (~10 nm). There may be a dependence of cluster size on Bi (and O) vacancies, but this could be masked by the multiple contributions to atom column intensity.

Refining the XRD data with bismuth deficiency is reasonable given the TEM-EDS analysis that suggested similar levels of Bi deficiency as were applied in the refinements [18]. Segregation of Bi at grain boundaries in the current 0.5BCT-0.5BMT ceramic, as shown by STEM-EDS mapping and from the increased contrast at grain boundaries in the ADF images of the thinned ceramic (Fig. 7) are in agreement with the matrix phase having a Bi deficit. The atomic percentage of Bi relative to all cations was estimated by semi-quantitative analysis of EDS spectra to be ~20 at% within grains and ~30 at% at the grain boundary regions i.e. there is a significant Bi deficiency within grains (Fig. 7). For comparison, the composition suggested by refinement of the HR-XRD

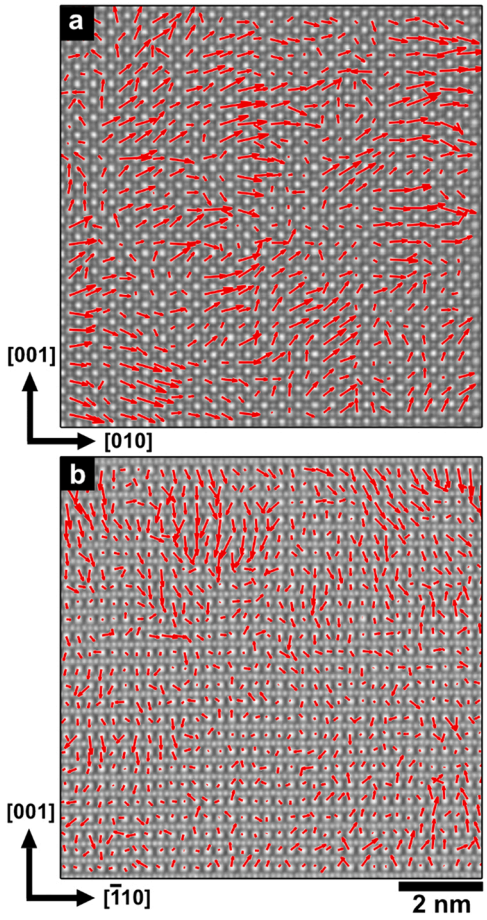

Fig. 5. 0.5BCT-0.5BMT average cation displacement dipole orientations across each unit cell shown with red arrows (arrow size proportional to displacement, but not to absolute scale) with respect to oxygen anions for samples oriented along the: (a) < 100 > and (b) < 110 > zone axes imaged by iDPC.

indicates 18 at% of the Bi sites are vacant (Table 1), corresponding to 21 at% Bi relative to all cations, whereas the nominal, stoichiometric composition of 0.5BCT-0.5BMT should give 25 at% Bi relative to all cations (i.e. implying 16 % Bi deficiency). Based on HR-XRD refinement the formula of the matrix corresponds to $Ba_{0.4}Ca_{0.1}Bi_{0.41-}Ti_{0.75}Mg_{0.25}O_{2.865}V_{Bix}V_{Oy}$, with x = 0.09 and y = 0.135, where x is the atom fraction of Bi vacancies and y the inferred oxygen vacancy content. However, the actual level of oxygen vacancies, may be lower than y = 0.135 due to 'superoxidation' during cooling from the sintering temperature. It is presumed that transport of Bi to grain boundaries occurs at elevated temperatures during synthesis as part of the evaporation process. Loss of Bi from the matrix due to evaporation occurs despite embedding sample pellets in an 'atmosphere' powder during sintering, as described in the Experimental section. The net result is a final matrix containing significant levels of A-site, Bi vacancies.

The uniformity of A-site column intensities in ADF images suggests a random distribution of Bi-vacancies. The presence of Bi *A*-site vacancies and oxygen vacancies, resulting from 'accidental' process-related bismuth oxide losses would be expected to perturb the local electrostatic and stress fields that control polarisation in relaxor dielectrics. Especially as each A-site cation is associated with eight BO_6 octahedra, the presence of $\sim 16-18$ at% (of randomised) Bi vacancies and their associated under-bonded oxygen atoms will have a significant influence on local structural distortions, including ion displacements. Thus, the dependence of polarisation on *B*-site cation displacements or distortions may be governed by simple nearest *A*-site and oxygen vacancy variations and would be consistent with the small ~2 nm polar regions identified in our polarization maps (Fig. 5). The results highlight an important aspect of polar nanostructure that has hitherto received little attention in the quest to understand mechanisms leading to a temperature -stable permittivity response; that of high levels of inferred ion vacancies. Ion vacancies could perturb the normal thermal evolution of polar nanostructure characteristic of a standard relaxor and so supress the diffuse permittivity peak in our heavily Bi modified relaxor dielectrics. This has not been considered in previous simulation work aimed at exploring the origins of the near-temperature stable permittivity-temperature response. In support of this possibility, it is noteworthy that inducing A-site vacancies in ferroelectric perovskite materials such as $NaNbO_3$ with A-site donor (M) dopants such as Gd^{3+} and Bi^{3+}, based on the mechanism $Na_{1-3x}M_xNbO_3$, have been shown to decrease and broaden the permittivity response [31,32]. This has also been attributed to nanoscale modulations of the lattice distortions [32].

The higher thermal parameter of Bi^{3+} ions relative to those of the other species in 0.5BCT-0.5BMT on both *A* and *B*-sites, (Table 1) is in agreement with a significant local disorder associated with the inferred ion vacancies. Bismuth ion hopping or rattling was proposed as the origin of the strong frequency dispersion observed in the temperature dependent dielectric $BiScO_3$-$BaTiO_3$ system [14]. Indeed asymmetric Bi-O and Pb-O bonding are well known phenomena, originating from an asymmetric hybridization of outer-core electron orbitals (*6p* and 6 *f*) of these metal ions [33,34]. The thermal displacement parameters of the Bi^{3+} ions in the 0.5BCT-0.5BMT structure derived from our refinements are very close to the B_{iso} factor of Pb^{2+} in cubic PZT at 300 °C, B_{iso}= 4.73 Å^2 (u_{iso}=0.245 Å), whereas the corresponding thermal

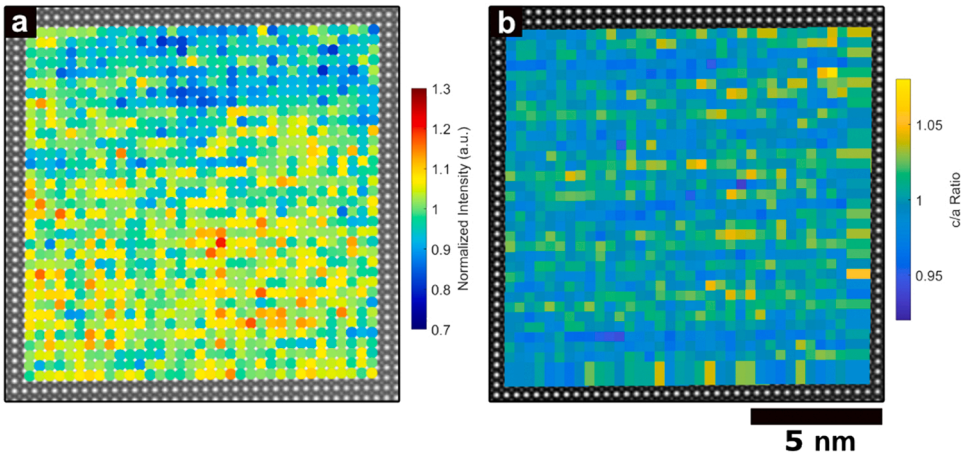

Fig. 6. (a) Normalized *B* sub-lattice atom column intensities of the < 100 > oriented 0.5BCT-0.5BMT and (b) c/a ratios for the *B* sub-lattice positions.

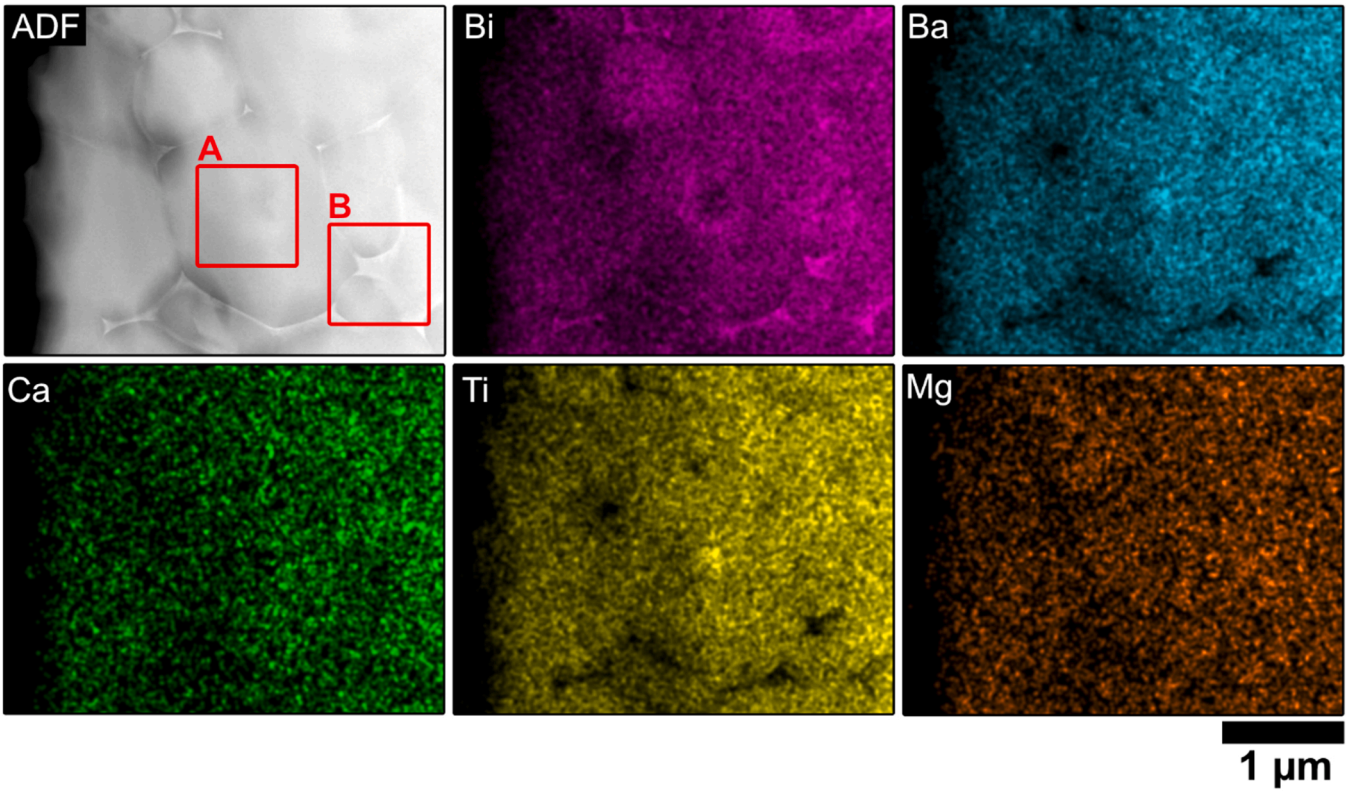

Fig. 7. Lower magnification ADF STEM image of the 0.5BCT-0.5BMT ceramic thin section (top left) with corresponding elemental, EDX maps showing segregation of Bi to grain boundaries. Regions A and B are used to quantify the Bi content in grain (A) and grain boundary (B) regions by integrating EDX spectra acquired from these regions and quantifying the Bi content relative to all cations.

displacement parameters for Pb^{2+} in rhombohedral PZT are B_{11} = 2.44 Å^2 (u_{11} =0.18 Å) at room temperature. (U = B/8π^2, U=<u^2 >) [35,36].

Overall, the current work suggests that the precise relationship between structure and properties, specifically the attenuation of the permittivity-temperature peak, in compositionally complex Bi-containing relaxor dielectrics may be controlled by the high level of vacancy defects in these ceramics, in addition to any longer range chemical heterogeneity [18]. The results indicate that in future the role of crystal vacancies be included in simulation based mechanistic studies as they could play a critical role in moderating the dielectric response of this class of material.

5. Conclusions

A combination of high-resolution synchrotron X-ray powder diffraction and advanced electron microscopy imaging and analysis techniques have been applied to examine the structure of the high temperature dielectric ceramic, $0.5Ba_{0.8}Ca_{0.2}TiO_3$-$0.5BiMg_{0.5}Ti_{0.5}O_3$. Average cation displacements relative to the oxygen ion positions were imaged using integrated differential phase contrast scanning transmission electron microscopy. The results indicated the existence of polar clusters, 2–5 nm in size. A high level of Bi vacancies was revealed by XRD refinements and by TEM-EDS analysis. The A-site vacancies in this class of material could be an important consideration in the ongoing quest to explain the mechanisms leading to the suppression of the peak in the relative permittivity-temperature response of a relaxor ferroelectric.

Declaration of Competing Interest

The authors declare that they have no known competing financial interests or personal relationships that could have appeared to influence the work reported in this paper.

Acknowledgements

The electron microscopy was performed at the Analytical Instrumentation Facility (AIF) at North Carolina State University, which is supported by the State of North Carolina and the National Science Foundation (award number ECCS-2025064). The AIF is a member of the North Carolina Research Triangle Nanotechnology Network (RTNN), a site in the National Nanotechnology Coordinated Infrastructure (NNCI). Other aspects of the work were performed as part of projects funded by UK Research Council at Leeds and Sheffield: award numbers EP/015514/1 and EP/P015565/1 respectively. Synchrotron XRD data were collected at Diamond Light Source UK. Andrew Rappe's visits to Leeds were funded by a Cheney Fellowship administered by the University of Leeds. J. Zhang. acknowledges the support of the Office of Naval Research, under grant N00014-20-1-2701, for the development of molecular dynamics models of temperature-stable relaxor ferroelectrics. A. M. R. acknowledges financial support by the U. S. Department of Energy, Office of Science, Office of Basic Energy Sciences Energy Frontier Research Centers program under Award Number DE-SC00211118. Thanks are expressed to Andrew Forsyth, University of Manchester for discussions on high-power capacitors. Valuable preliminary experiments were conducted in collaboration with David Hernandez-Maldonado (Universidad Complutense Madrid), Ian MacLaren (University of Glasgow) and Mike Ward (Gatan plc).

References

[1] W. Lee, S. Li, D. Han, B. Sarlioglu, T.A. Minav, M. Pieto, Review of integrated motor drive and wide-bandgap power electronics for high-performance electro-hydrostatic actuators, IEEE Trans. Transp. Electrification 4 (2018) 684–693.

[2] J. Watson, G. Castro, A review of high-temperature electronics technology and applications, J. Mat. Sci: Elect. 26 (2015) 9226.
[3] H. Ogihara, C.A. Randall, S. Trolier-McKinstry, Weakly coupled relaxor behavior of $BaTiO_3$-$BiScO_3$ ceramics, J. Am. Ceram. Soc. 92 (2009) 110–118.
[4] S. Wada, K. Yamato, P. Pulpan, N. Kumada, B.-Y. Lee, T. Iijima, C. Moriyoshi, Y. Kuroiwa, Piezoelectric properties of high Curie temperature barium titanate–bismuth perovskite-type oxide system ceramics, J. Appl. Phys. 108 (2010), 094114.
[5] A. Zeb, S.J. Milne, Low variation in relative permittivity over the temperature range 25–450 °C for ceramics in the system (1-x)[Ba0.8Ca0.2TiO3]-x[Bi (Zn0.5Ti0.5)O3], J. Eur. Ceram. Soc. (34) (2014) 1727–1732.
[6] B. Peng, Q. Zhang, G. Bai, G.J.T. Leighton, C. Shaw, S.J. Milne, Z. Gao, B. Zou, H. Huang, Z. Wang, Phase-transition induced giant negative electrocaloric effect in a lead-free relaxor ferroelectric thin film, Energy Environ. Sci. 12 (2019) 1708–1717.
[7] R.A. Cowley, S.N. Gvasaliya, S.G. Lushnikov, B. Roessli, G.M. Rotaru, Relaxing with relaxors: a review of relaxor ferroelectrics, Adv. Phys. 60 (2011) 229–327.
[8] A.A. Bokov, Z.G. Ye, Recent progress in relaxor ferroelectrics with perovskite structure, J. Mater. Sci. 41 (2006) 31–52.
[9] G. Burns, F.H. Dacol, Crystalline ferroelectrics with glassy polarization behavior, Phys. Rev. B 28 (1983) 2527–2530.
[10] P.M. Gehring, S.-E. Park, G. Shirane, Soft phonon anomalies in the relaxor ferroelectric Pb (Zn 1/3 Nb 2/3)$_{0.92}$Ti$_{0.8}$O$_3$, Phy. Rev. Letts (84) (2000) 5216.
[11] H. Takenaka, I. Grinberg, A.M. Rappe, Anisotropic local correlations and dynamics in a relaxor ferroelectric, Phys. Rev. Lett. 110 (2013), 147602.
[12] M. Matsuura, K. Hirota, P.M. Gehring, Z.G. Ye, W. Chen, G. Shirane, Composition dependence of the diffuse scattering in the relaxor ferroelectric compound, (1-x)Pb ($Mg_{1/3}Nb_{2/3}O_3$-xPbTiO$_3$ (0≤ x ≤0.40), Phys. Rev. B 74 (2006), 144107.
[13] H. Takenaka, I. Grinberg, S. Liu, A.M. Rappe, Slush-like polar structures in single-crystal relaxors, Nature 546 (2017) 391–395.
[14] V. Krayzman, I. Levin, J.C. Woicik, F. Bridges, Correlated rattling-ion origins of dielectric properties in reentrant dipole glasses $BaTiO_3$-$BiScO_3$, Appl. Phys. Lett. 107 (2015), 192903.
[15] I. Levin, V. Krayzman, J.C. Woicik, F. Bridges, G.E. Sterbinsky, T.-M. Usher, J.-L. Jones, D. Torrejon, Local structure in $BaTiO_3$-$BiScO_3$ dipole glasses, Phys. Rev. B 93 (2016), 104106.
[16] T.-M. Usher, T. Iamsasri, J.S. Forrester, N. Raengthon, N.M. Triamnak, D.P. Cann, J.L. Jones, Local and average structures of $BaTiO_3$-Bi($Zn_{1/2}Ti_{1/2}$)O_3, J. Appl. Phys. 120 (2016), 184102.
[17] A. Zeb, S.J. Milne, Stability of high-temperature dielectric properties for (1−x) $Ba_{0.8}Ca_{0.2}TiO_3$–xBi($Mg_{0.5}Ti_{0.5}$)O_3 ceramics, J. Am. Ceram. Soc. 96 (2013) 2887–2892.
[18] T. Roncal-Herrero, J. Harrington, A. Zeb, S.J. Milne, A.P. Brown, Nanoscale compositional segregation and suppression of polar coupling in a relaxor ferroelectric, Acta Mater. 158 (2018) 422.
[19] M. Voyles, J.L. Grazul, D.A. Muller, Imaging individual atoms inside crystals with ADF-STEM, Ultramicroscopy 96 (2003) 251–273.
[20] C. Ophus, J. Ciston, C.T. Nelson, Correcting nonlinear drift distortion of scanning probe and scanning transmission electron microscopies from image pairs with orthogonal scan directions, Ultramicroscopy 162 (2016) 1–9.
[21] X. Sang, A.A. Oni, J.M. LeBeau, Atom column indexing: atomic resolution image analysis through a matrix representation, Microsc. Micro 20 (2014) 1764–1771.
[22] M. Nord, P.E. Vullum, I. MacLaren, T. Tybell, R. Holmestad, Atomap: a new software tool for the automated analysis of atomic resolution images using two-dimensional Gaussian fitting, Adv. Struct. Chem. Imaging 3 (2017) 1.
[23] I. Lazić, E.G.T. Bosch, S. Lazar, Phase contrast STEM for thin samples: Integrated differential phase contrast, Ultramicroscopy 160 (2016) 265.
[24] X. Sang, E.D. Grimley, C. Niu, D.L. Irving, J.M. Lebeau, Direct observation of charge mediated lattice distortions in complex oxide solid solutions, Appl. Phys. Lett. 106 (2015), 061913.
[25] F. Li, et al., Giant piezoelectricity of Sm-doped Pb(Mg1/3Nb2/3)O3-PbTiO3 single crystals, Science 364 (2019) 264–268.
[26] P.M. Voyles, D. a Muller, J.L. Grazul, P.H. Citrin, H.-J.L. Gossmann, Atomic-scale imaging of individual dopant atoms and clusters in highly n-type bulk Si, Nature 416 (2002) 826–829.
[27] M.J. Cabral, S. Zhang, E.C. Dickey, J.M. Lebeau, Gradient chemical order in the relaxor Pb(Mg1/3Nb2/3)O3, Appl. Phys. Lett. 112 (2018), 082901.
[28] A.D. Hilton, D.J. Barber, C.A. Randall, T.R. Shrout, On short range ordering in the perovskite lead magnesium niobate, J. Mater. Sci. 25 (1990) 3461.
[29] A.D. Hilton, C.A. Randall, D.J. Barber, T.R. Shrout, TEM studies of Pb(Mg1/3Nb2/3)O3-PbTiO 3 ferroelectric relaxors, Ferroelectrics 93 (1989) 379.
[30] M.J. Krogstad, et al., The relation of local order to material properties in relaxor ferroelectrics, Nat. Mater. 17 (2018) 718–724.
[31] I.P. Raevski, S.A. Prosandeev, A new, lead free, family of perovskites with a diffuse phase transition: $NaNbO_3$-based solid solutions, J. Phys. Chem. Solids 63 (2002) 1939.
[32] I. Levin, F. Yang, R. Maier, W.J. Laws, D.S. Keeble, G. Cibin, D.C. Sinclair, Displacive order–disorder behaviour and intrinsic clustering of lattice distortions in Bi-substituted $NaNbO_3$, Adv. Funct. Mater. 30 (2020) 2001840.
[33] P.A. Cox, R.G. Egdellt, J.B. Goodenough, A. Hamnett, C.C. Naish, The metal-to-semiconductor transition in ternary ruthenium (IV) oxides: a study by electron spectroscopy, J. Phys. C: Solid State Phys. 16 (1983) 6221–6239.
[34] J.B. Goodenough, J.M. Longo, Crystallographic and magnetic properties of perovskites and perovskite-related compounds, in: K.-H. Hellwege (Ed.), Landolt-Börnstein Numerical Data and Functional Relationships in Science and Technology, New Series. Group III: Crystal and Solid State Physics: Vol. 4, Magnetic and Other Properties of Oxides and Related Compounds, Part A, Springer, Berlin, Heidelberg, New York, 1970, p. pp144.
[35] H. Yokota, N. Zhang, P.A. Thomas, A.M. Glazer, Crystal structure determinations of Zr Rich-$PbZr_{1-x}$ Ti $_x$ O_3, Ferroelectrics 414 (2011) 147–154.
[36] A.M. Glazer, S.A. Mabud, R. Clarke, Powder profile refinement of lead zirconate titanate at several temperatures. I. PbZr0.9Ti0.1O3, Acta Cryst., B34 1060–1065.